Three-dimensional flow assessment of microvascular beds with interstitial space

Navaneeth Krishna Rajeeva Pandian[1,2], Alanna Farell[1,2], Emily Davis[1,2], Jessica Li Chang Teo[1,2], Subramanian Sundaram[1,2], Jeroen Eykmans[1,2], and Christopher S Chen[1,2]

[1] Harvard Wyss Institute for Biologically Inspired Engineering, Boston, MA 02115, USA
[2] Biological Design Center, Department of Biomedical Engineering, Boston University, Boston, MA 02215, USA;

Abstract:
Microvascular networks take shape from the inherent flow, forces, and nutrient requirements of the tissue. These remarkably fluid flow-related forces are difficult to measure experimentally and are usually derived from flow values measured during experiments. Currently, there are no 3D vascular flow assessment tools and associated forces. Hence, we developed an algorithm to analyze microvascular networks, which can give morphological parameters such as the network architecture, individual diameters of the vessels, and their tortuosity. These parameters are then used to model the network bottom-up in computational software, including the vessel, endothelial lining, and interstitial space. We observe that including the endothelial monolayer with higher permeability than the surrounding hydrogel makes a marked change in the flow profiles and magnitudes. Further, we show that including a growth factor such as VEGFA helps microvascular networks mature, and the change in overall dimensions and shape of the network changes the forces they encounter. This tool can find varying applications, from in-vitro models to in vivo disease models.

Introduction: Continuous blood flow is required through the blood vascular network in the body for the constant supply of oxygen, nutrients, and immune cells to the tissues. This flow inherently applies shear and hydrostatic forces on the vessels' endothelium lining, leading to the overall vessel size, network architecture, and endothelial cell behavior. Blood vessels are critical conduits in the body that help transport blood and nutrients to different body parts. The blood vessel network architecture and individual diameters depend on the tissue's oxygen, nutrients, and immune cell requirements [1, 2]. Flowing blood applies different forces (like wall shear, hydrostatic pressure, etc.) on the endothelial cells lining the microvascular blood vessels and can alter their phenotype [3]. Deviation (increase or decrease) of these forces from an optimal value can lead cells to a pathological phenotype [4, 5].

These forces cannot be directly measured from blood vessel experiments and can only be derived from these vessels' flow or deformations and their profiles and magnitudes [6]. Due to the inherent difficulty in measuring flow, maintenance, and cost incurred, animal models are not preferred for such studies. In vitro models, such as microfluidic models, are heavily depended on to study flow effects on microvascular networks. Though many microfluidic models are currently available to study the effects of flow on microvascular networks, there are minimal tools to measure the exact velocity of flow and forces acting on the micro-vessels of these networks [7-9]. Currently, in most studies, the networks are characterized only for their architecture, network density, average vessel diameter, average tortuosity of vessels, etc. [8, 10-12]. Though some analysis pipelines have come up that can calculate the velocity profiles and wall shear stresses in the vessel networks, they either use the truncated 2D models [13, 14] or do not include the interstitial space [15, 16]. 2D truncated models rely on projecting 3D networks into a plane, leading to data loss such as changes in diameter, branch points, etc. Flow fields in 3D networks have a velocity component in the third dimension, which is neglected in 2D truncated models. Models, including interstitial space, use a generalized porosity and permeability value for the interstitial space and do not include the endothelial monolayer and its porosity and permeability. The endothelial monolayer has lower porosity and permeability values than the interstitial space, which cannot be neglected. [17, 18]. Moreover, no 3D vascular network CFD models exist, including interstitial space and/or endothelial lining thickness. Currently, 3D segmentation tools are available. However, those models cannot be directly used for CFD analysis due to the complex geometry features that must be corrected for the later CFD analysis, and it is challenging to generate the interstitial space for analysis owing to the self-interfering nature of the vessel networks. [19-22]. To overcome this limitation, we model the network bottom-up from the network parameters derived from the 3D image stack in an analysis software that can handle 3D modeling (currently, Matlab has limited 3D modeling capabilities).

We establish an analysis pipeline to estimate the velocities and forces acting on a 3-D in-vitro vessel network by solving the flow equations in a 3-D domain. The model also incorporates the endothelial monolayer thickness of the vessels and interstitial space of the tissue, which are currently not considered in the literature. We use image processing algorithms in Matlab that automatically segment the 3D confocal image stack and get the network elements' diameters, lengths, and connectivity (overall architecture). The above parameters are used to build the network from a bottom-up approach in the analysis software (Comsol). We use a combination of

Boolean operations to rebuild the network, the endothelial monolayer lining the network, and the interstitial space in the analysis software. Thus, the model includes the porosity and permeability values of the endothelial lumen and interstitial space (biomaterial). We solve for the flow equations in networks, interstitial space, and the endothelial monolayer thickness and compare the predicted velocity values with the experiments to validate our model.

Results:

Flow in the vessel alters due to interstitial space and endothelial lumen: To check our hypothesis that the presence of interstitial space and endothelial lumen will affect the overall flow and forces in the vessel, we conducted perfusion experiments in single-channel devices (Figure 1a). We culture endothelial cells in the needle drive hollow channels formed in the device's hydrogel (fibrin in this case) for three days till confluent. Once confluent, the channels were perfused with fluorescently tagged Dextran and microbeads (approx. 15 um diameter, Figure 1 b). The microbead motion is captured to calculate the velocity profile of the flow in the vessel. We model the hydrogel space and the hollow lumen of the microfluidic chip to numerically calculate the flow profiles under different conditions (Figure 1c). We observe that when the lumen in the hydrogel is modeled as a pipe with no leakage, the model predicts a higher velocity than the actual experimental value (Figure 1d). Interestingly, assuming the bulk hydrogel to have either fibrin or endothelial monolayer permeability leads to further deviation in the prediction of flow velocity and its profile. Using a leaky pipe model leads to lower deviation in velocity experimental results, but the wall shear stress prediction deviates from the original value (Figure 1.d). The model, including the fibrin and endothelial monolayer thickness, shows that the fluid entering the device enters and seeps into the fibrin hydrogel and, in turn, seeps out at the outlet. Finally, flow profile and magnitude in the hydrogel space also show marked differences when the endothelial monolayer is modeled instead of generalized hydrogel or endothelial monolayer permeability to the whole model.

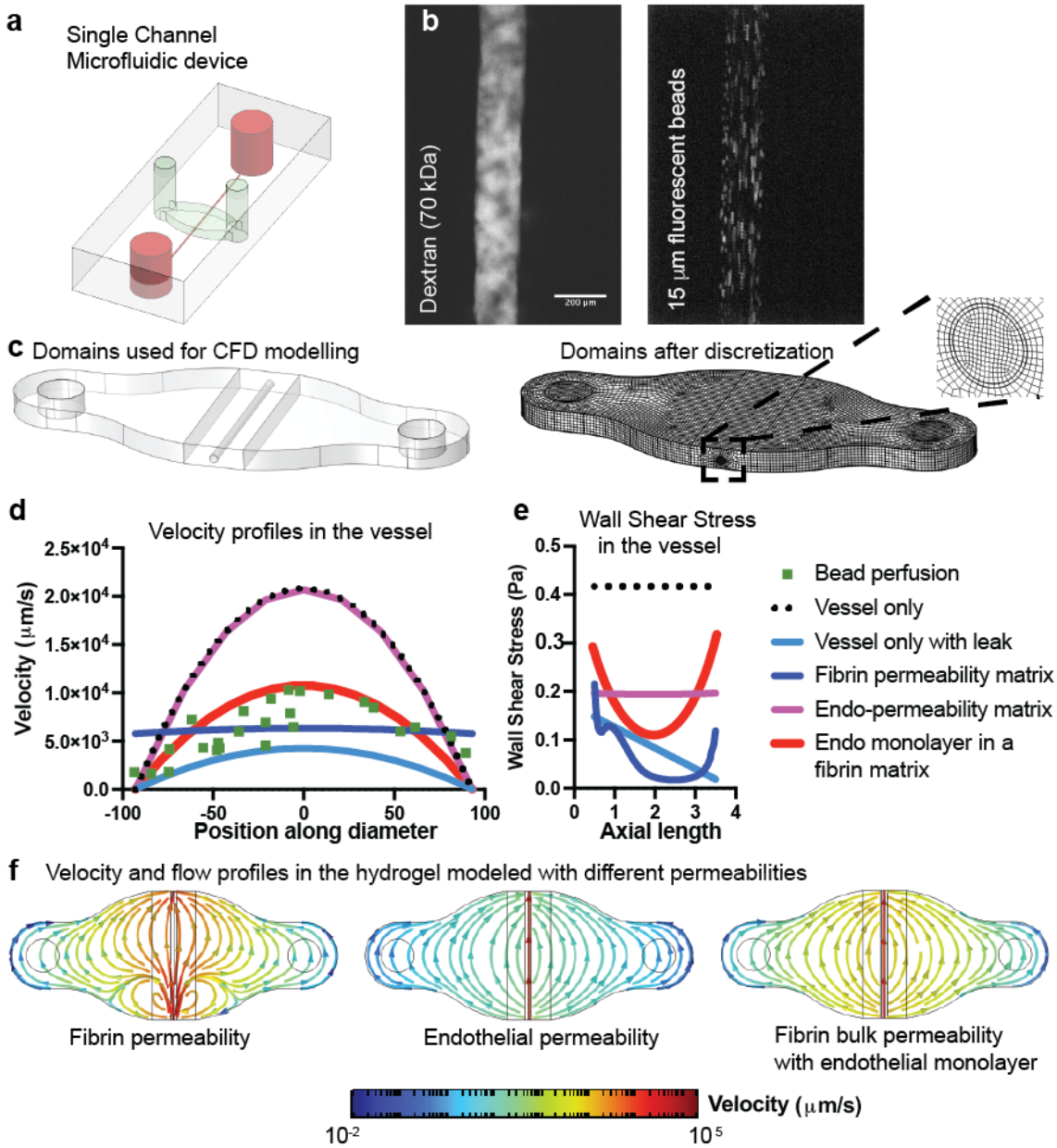

Figure 1: Modeling endothelial lumen and hydrogel permeability in a single channel device. a) illustration of a single-channel device. b)micrographs showing the perfusion of dextran and microbeads through the single-channel device. C) The numerical model uses the hydrogel region to assess the flow patterns, the model's discretized form, and the endothelial monolayer included in the model. D) Different modeling assumptions predict different velocity profiles in the vessel. E) These assumptions also affect the wall shear stress predictions. F) the flow profiles in the single-channel device hydrogels are also different.

Pipeline to model and analyze microvascular networks: We image in vitro microvascular networks formed in the microfluidic devices using confocal microscopy. These images are stacks containing different depth positions. Generally, these images are taken of the fluorescently tagged dextran perfused through the network or the surface markers such as lectin stained in the network. Both image sets can be used for the assessment and modeling explained in this work. The aspect ratio of each image stack is adjusted such that the voxels are equally sized in all directions. The script has a user interface that helps generate binary images of the complete

vascular network from the 3D image stack. An additional contrast-limited adaptive histogram equalization (CLAHE) [8] algorithm is run for lectin-only channels, which can have large signal loss with a volume depth. Next the segmentation of the binarized image is done directly using the thresholding specified by the user (for the Dextran channel) or by a refinement algorithm of distance regularized level set evolution (DRLSE) with a double well potential for weaker signals (such as lectin).

The segmentation generates the 3D medial axis skeleton using homotopic thinning [23]. This is further converted into a graph containing links representing the vessel structures and nodes to identify the vessel's branching and terminal points. The vessel radii are calculated based on the distance between the surface and the medial skeleton of the graph links, and the mean diameters for all vessels, as well as only perfused vessels, are reported. After obtaining the vessel morphological parameters, we use a Java (programming language) based algorithm to build the entire network in COMSOL using primitive building blocks such as cylinders, spheres, and blocks. Once the model is built in COMSOL with vessel structure, endothelial-monolayer, and interstitial space, we apply appropriate boundary conditions and physics to solve the flow equations in free flow and porous media to get the flow profiles and forces in the network and its interstitial space.

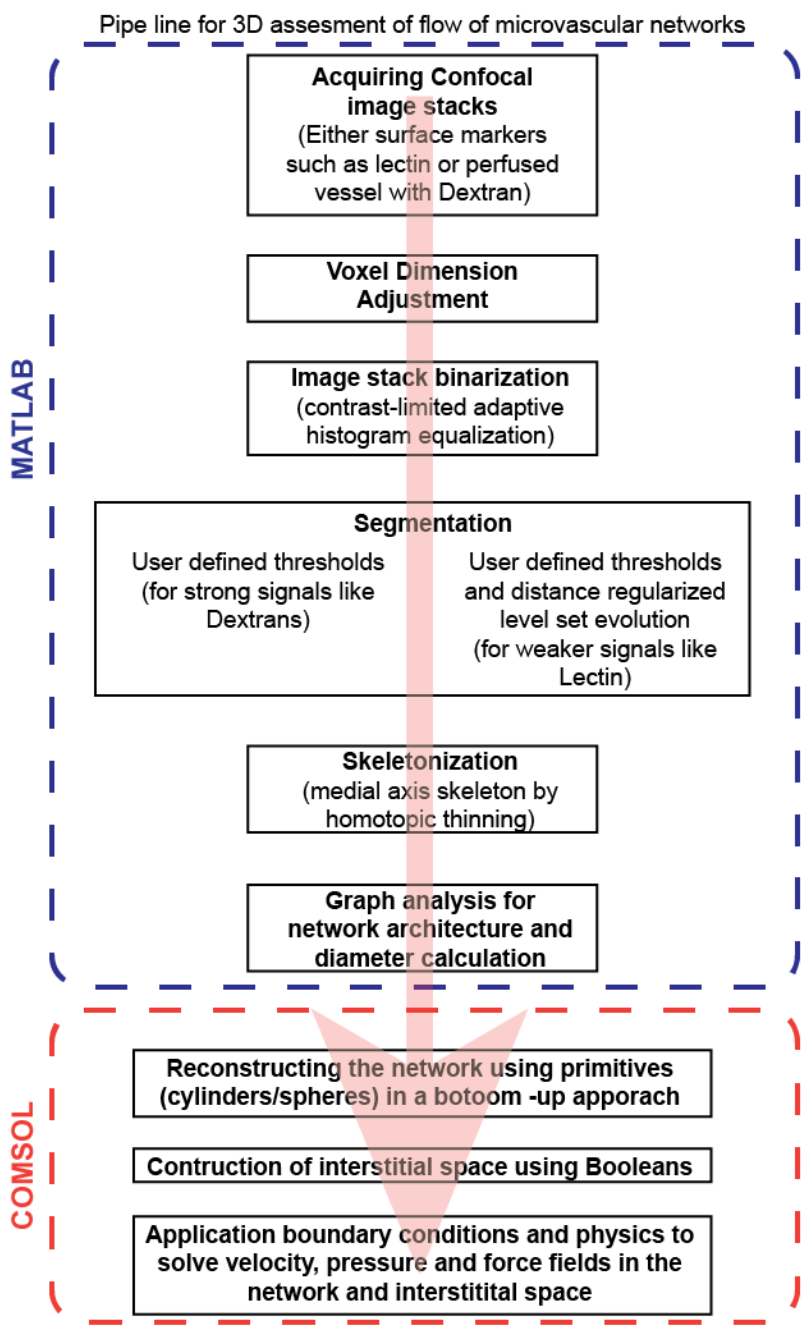

Figure 2: Pipeline for flow assessment in microvascular networks. The acquired confocal image stack is run through a. series of operations written in Matlab to attain the morphological parameters that define the shape and architecture of the network. This morphological parameter are then used to build the network bottom up in Comsol and solved to get the flow patterns in the device.

Validating the models generated: We validate the models generated using the algorithm in two ways. First, we compare the diameters computed by the algorithm with the ground truth value of manual measurement and existing algorithms widely used in the fields. We observe our

algorithm to give closer values (rms value 0.9965 for eight independent random vessels from networks) to the ground truth compared to other algorithms. This may be due to the 2D nature of assessment used in the other algorithms when we use the 3D algorithm. Next, we compare the overall architecture of the model generated in Comsol to the initial segmentation of the image. We compare two aspects in this check where first we check the deviation of surfaces (root mean square value) of the comsol model to the segmentation. The deviation in the surface points falls below 20%, and less than 1% of the points compared have deviations more than 5% in our approach. Next, we compare the volume of the Comsol model to the volume of the segmentation created, and we get a root mean square value of 0.9418.

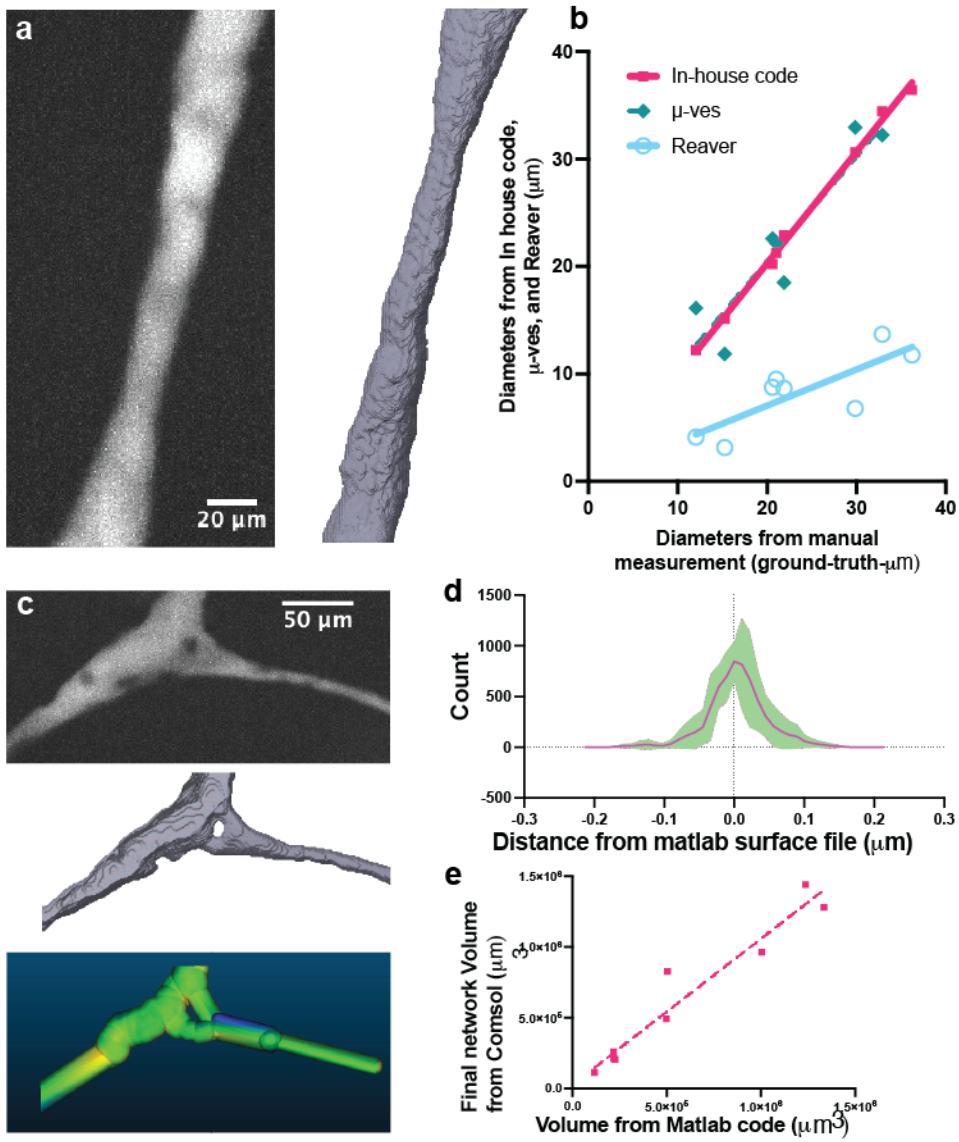

Figure 3 Comparison of morphological parameters of the algorithm-generated network. A) Image of a vessel perfused with dextran from the whole network and its segmented part. B) Graph comparing the diameters measured manually to different algorithms (algorithm used in this work, µ-ves and REAVER).c) A bifurcated vessel in the image, after segmentation and after comsol buildup,. D) Graph showing the deviation of points on the surface of the comsol model and the segmentation. E) Graph showing the comparison of volumes of the comsol model and segmentation.

Assessment of in-vitro microvascular networks: We cultured human umbilical vein endothelial cells (HUVECs) with human lung fibroblasts in a two-channel microfluidic device already used in our lab. We culture these devices for seven days to form microvascular networks that span from one end of the device to the other. We treated some of the devices with a potent growth factor known as vascular endothelial growth factor A (VEGF-A). While in bigger mature vessels, VEGFA is known to lower the barrier function, in immature growing vessels, VEGFA is known to mature the vessels, thereby increasing the overall diameter of the vessel network. We observe the second phenomenon, where our networks become immature and mature under VEGF-A treatment. We observe that the average diameter of the VEGF-A treated vessels is greater than that of the control devices. We built these networks in Comsol and solved the fluid flow equations to obtain these devices' average velocity and wall shear rates. Our models could predict lower velocities in the VEGF-A-treated devices with larger diameters. These lowering of velocities also resulted in the lowering of overall traction forces in these networks as the wall shear rate directly calculated from the flow velocity was also lower than that of the control.

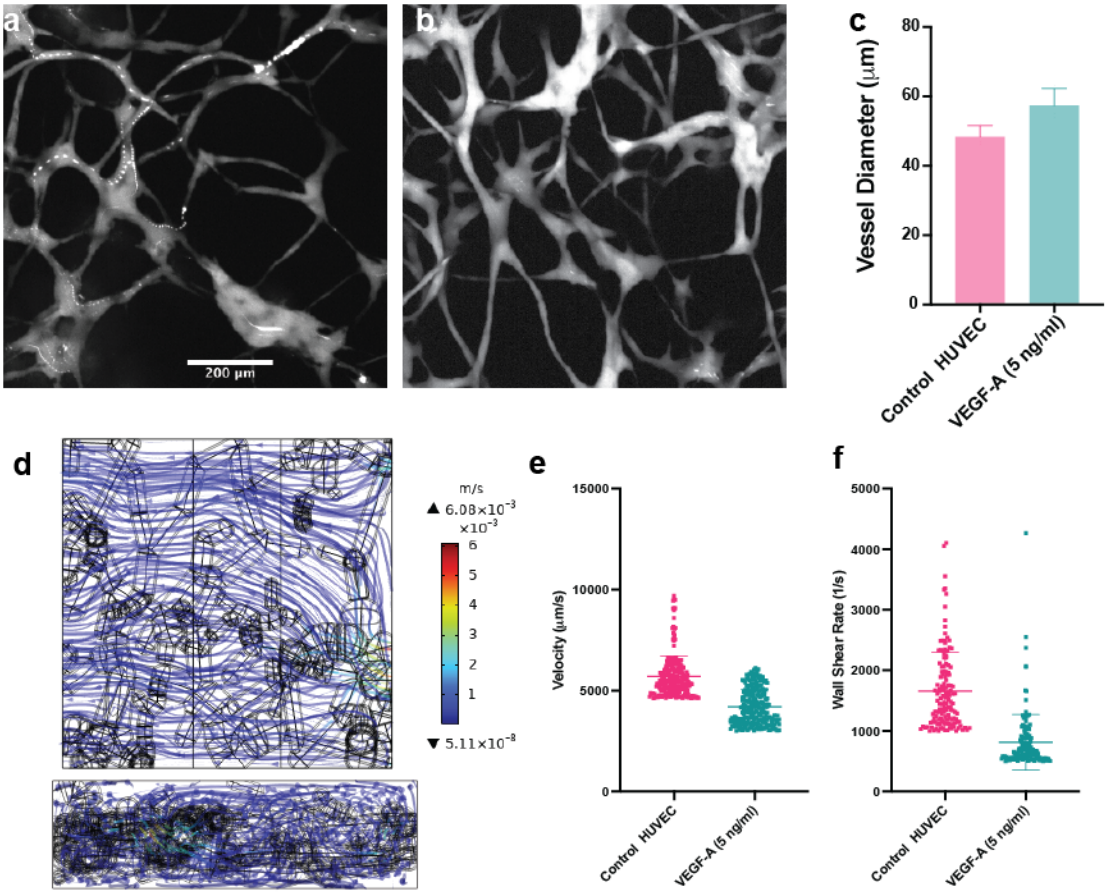

Figure 4: Assessment of in vitro microvascular networks. A) micrograph showing a control microvascular network perfused with dextran. B)) micrograph showing a microvascular network treated with VEGF-A perfused with dextran. C) The graph shows the difference in average diameters of vessels in three devices treated with VEGF-A and controls. D) Micrograph showing the flow streamlines in one of the models solved for flow equations. E) Graph showing the difference in velocity in the VEGF-A treated and control microvascular networks. F) Graph showing the difference in wall shear rate in the VEGF-A treated and control microvascular networks

Discussion: This is the first demonstration of the CFD analysis of in-vitro vascular networks that model the 3D microvascular network, its interstitial space, and the endothelial monolayer barrier. Modeling interstitial space is essential as it helps capture fluid leakage from the microvascular network and into the network from interstitial space when external interstitial pressure is higher in in-vitro systems. Modeling interstitial space is essential in future studies. Our approach can be used to study drug, nutrient, or oxygen transport in the parenchyma of in vivo tissues or interstitial space in vitro systems. We have modeled the endothelial monolayer separately, as the permeability of the monolayer is higher than the interstitial space. Modeling the monolayer is crucial as the difference in permeability values affects the velocity profile in the microvascular network and the interstitial space. However, the inclusion of the endothelial monolayer increases the computational cost. The model can be generated from dextran-perfused vessels or vessels marked for endothelial markers such as lectin or fluorescently tagged endothelial cells. The model can solve the flow of in vivo 3D microvasculature, including its interstitial space (flow in brain slices, not shown here).

Like any other model, our model has some limitations; we model the vessels with perfectly rounded cross-sections, whereas the original network vessels have an elliptical cross-section. However, modeling elliptical cross sections has drawbacks, such as a lot of model cleanup for proper discretization. We do not include the exact flow boundary conditions at the interstitial space boundaries due to the limitations of measuring the exact inflow/outflow conditions in the hydrogels experimentally. Monolayer thickness is assumed to save modeling time rather than taking the exact thickness of the endothelial lumen at different places. We can easily implement this, but not in this initial work.

Overall, this work helps model and analyze 3D vascular networks that can be used in different in vitro and in vivo settings. The model includes microvascular networks, endothelial monolayer, and the tissue's interstitial space, an important fluid transport mode in invitro and in vivo systems. Our approach opens the door for examining transport between blood and lymphatics, where the flow predominantly happens through the interstitial space.

Methods:

Microvascular Network generation: The molds for the 2-channel microfluidic devices were developed using stereolithography (Proto Labs). Polydimethylsiloxane (PDMS) was mixed at 1:10 ratio and poured on the mold, and cured overnight at 60°C. Individual devices were cut, plasma treated, and bonded to coverslips. To enhance hydrogel bonding to PDMS, the surface inside the device was functionalized with 0.01% poly-L-lysine and 1% glutaraldehyde following plasma activation and washed overnight in DI water. The devices were dried at 100°C for 15 minutes. Acupuncture needles (300 µm diameter) (Hwato) were blocked in 0.1% (w/v) bovine serum albumin (BSA) (Sigma) in phosphate buffer saline (PBS) for 45 minutes and inserted through the two needle guides. Devices with needles were UV-sterilized for 15 minutes.

Both HUVECs and Human lung fibroblasts (HLFs) were lifted from culture plates using Trypsin (.25%), centrifuged at 200 g for 4 minutes, and resuspended to a concentration of HUVECs- 8.78

million cells/mL in EGM-2 and HLFs – 2.7 million cells/ml. A solution of HUVECs (3 million cells/mL), HLFs (1 million), fibrinogen (2.5 mg/mL), and thrombin (1 U/mL) in EGM-2 was prepared for the bulk hydrogel region of each device. After the addition of thrombin, the solution was quickly injected into the tissue chamber, and the devices were repeatedly rotated while the solution was cross-linked. Appropriate media was added to each well of the device and placed in the incubator (37°C, 5% CO2). After 15 minutes, the needles were carefully ablated from the devices to create 300 µm hollow channels between the wells. Each device channel was seeded with additional HUVECs at 2 million cells/mL for at least 5 minutes on each side (top and bottom) in the incubator. Each device received 200 µL of appropriate media daily and cultured on the rocker inside the incubator.

Single-channel device preparation: The molds for the single-channel microfluidic devices were developed using stereolithography (Proto Labs). Polydimethylsiloxane (PDMS) was mixed at 1:10 ratio and poured on the mold, and cured overnight at 60°C. Individual devices were cut, plasma treated, and bonded to coverslips. To enhance hydrogel bonding to PDMS, the surface inside the device was functionalized with 0.01% poly-L-lysine and 1% glutaraldehyde following plasma activation and washed overnight in DI water. The devices were dried at 100°C for 15 minutes. Acupuncture needles (160 µm diameter) (Hwato) were blocked in 0.1% (w/v) bovine serum albumin (BSA) (Sigma) in phosphate buffer saline (PBS) for 45 minutes and inserted through the two needle guides. Devices with needles were UV-sterilized for 15 minutes. A solution of fibrinogen (2.5 mg/mL), and thrombin (1 U/mL) in EGM-2 was prepared for the bulk hydrogel region of each device. After the addition of thrombin, the solution was quickly injected into the tissue chamber. After 15 minutes, the needles were carefully ablated from the devices to create 300 µm hollow channels between the wells. Each device channel was seeded with additional HUVECs at 2 million cells/mL for at least 5 minutes on each side (top and bottom) in the incubator. Each device received 200 µL of appropriate media daily and cultured on the rocker inside the incubator.

Imaging: Devices were fixed using 4% PFA for 15 minutes on a rocker and washed with PBS overnight at 4°C. The devices were then blocked in 3% BSA overnight at 4°C. Lectin (UEA DyLight 649, Vector Labs) was diluted in the PBS at 1:100 and added to the devices and incubated at 4°C overnight. Devices were washed with PBS and image.

Just before imaging, 50 ul of 2000 kDa fluorescein isothiocyanate (FITC)-conjugated dextran (0.25 mg/mL) was added to one of the microfluidic channels to generate a pressure gradient between the two channels of the device. All device images were then captured by a Leica SP8 confocal microscope (Leica, Wetzlar, Germany) using a Leica 10x/0.30NA W U-V-I WD-3.60 and Leica LAS X imaging software. Bead perfusion experiments were conducted on a Andor Dragonfly spinning disk confocal microscope, with 10x air objective.

Image analysis: Images were analysed or converted and cropped to uniform sizes using imagej fiji software before being used in the matlab software. No other image preparation was done in this manuscript.

Flow equations: We solve for the Flow in the free channel described by the stationary, incompressible Navier-Stokes equations:

$$\rho(\mathbf{u}\cdot\nabla)\mathbf{u} = -\nabla\cdot[-p\mathbf{I} + \mu(\nabla\mathbf{u} + (\nabla\mathbf{u})^T)]$$
$$\nabla\cdot\mathbf{u} = 0$$

where μ denotes the dynamic viscosity (Pa·s), u refers to the velocity in the open channel (m/s), ρ is the fluid's density (kg/m3), and p is the pressure (Pa). In the porous domain, we solve for the Brinkman equations with Forchheimer correction describe the flow:

$$\frac{1}{\varepsilon_p}\rho(\mathbf{u}\cdot\nabla)\mathbf{u}\frac{1}{\varepsilon_p} = \nabla\cdot\left[-p\mathbf{I} + \frac{\mu}{\varepsilon_p}(\nabla\mathbf{u} + (\nabla\mathbf{u})^T)\right] - \left(\frac{\mu}{\kappa} + \frac{\rho\varepsilon_p C_f}{\sqrt{\kappa}}|\mathbf{u}|\right)\mathbf{u}$$
$$\rho\nabla\cdot\mathbf{u} = 0$$

Statistical Testing: For all experiments, independent two-sample populations (for example, lymphedema-on-chip and regular chips) will be compared using unpaired, two-sample t-tests with a normal distribution assumption. For group analyses, one-way ANOVA with Tukey's HSD (Honestly Significant Difference) tests will be used to compare the mean values. *$P < 0.05$ will be considered statistically significant. Statistical analyses will be performed using graphpad prism software.

Funding and acknowledgments:
This work is supported by funding from the Wellcome Leap HOPE Program.

References:

1. Fleischer, S., D.N. Tavakol, and G. Vunjak-Novakovic, *From arteries to capillaries: approaches to engineering human vasculature.* Adv Funct Mater, 2020. **30**(37).
2. Jacob, M., D. Chappell, and B.F. Becker, *Regulation of blood flow and volume exchange across the microcirculation.* Crit Care, 2016. **20**(1): p. 319.
3. Campinho, P., A. Vilfan, and J. Vermot, *Blood Flow Forces in Shaping the Vascular System: A Focus on Endothelial Cell Behavior.* Front Physiol, 2020. **11**: p. 552.
4. Dolan, J.M., J. Kolega, and H. Meng, *High wall shear stress and spatial gradients in vascular pathology: a review.* Ann Biomed Eng, 2013. **41**(7): p. 1411-27.
5. Hahn, C. and M.A. Schwartz, *Mechanotransduction in vascular physiology and atherogenesis.* Nat Rev Mol Cell Biol, 2009. **10**(1): p. 53-62.
6. Gates, P.E., et al., *Measurement of Wall Shear Stress Exerted by Flowing Blood in the Human Carotid Artery: Ultrasound Doppler Velocimetry and Echo Particle Image Velocimetry.* Ultrasound Med Biol, 2018. **44**(7): p. 1392-1401.
7. Margolis, E.A., et al., *Stromal cell identity modulates vascular morphogenesis in a microvasculature-on-a-chip platform.* Lab Chip, 2021. **21**(6): p. 1150-1163.
8. Song, H.G., et al., *Transient Support from Fibroblasts is Sufficient to Drive Functional Vascularization in Engineered Tissues.* Adv Funct Mater, 2020. **30**(48).
9. Wan, Z., et al., *A robust vasculogenic microfluidic model using human immortalized endothelial cells and Thy1 positive fibroblasts.* Biomaterials, 2021. **276**: p. 121032.

10. Aw, W.Y., et al., *Microphysiological model of PIK3CA-driven vascular malformations reveals a role of dysregulated Rac1 and mTORC1/2 in lesion formation.* Sci Adv, 2023. **9**(7): p. eade8939.
11. Ngo, M.T., J.N. Sarkaria, and B.A.C. Harley, *Perivascular Stromal Cells Instruct Glioblastoma Invasion, Proliferation, and Therapeutic Response within an Engineered Brain Perivascular Niche Model.* Adv Sci (Weinh), 2022. **9**(31): p. e2201888.
12. Whisler, J., et al., *Emergent mechanical control of vascular morphogenesis.* Sci Adv, 2023. **9**(32): p. eadg9781.
13. Bender, R.H.F., et al., *A vascularized 3D model of the human pancreatic islet for ex vivo study of immune cell-islet interaction.* bioRxiv, 2021: p. 2021.12.21.473744.
14. Mathur, T., J.J. Tronolone, and A. Jain, *AngioMT: An in silico platform for digital sensing of oxygen transport through heterogenous microvascular networks.* bioRxiv, 2023: p. 2023.01.09.523275.
15. Haase, K., et al., *Physiologic flow-conditioning limits vascular dysfunction in engineered human capillaries.* Biomaterials, 2022. **280**: p. 121248.
16. Rota, A., et al., *A three-dimensional method for morphological analysis and flow velocity estimation in microvasculature on-a-chip.* Bioeng Transl Med, 2023. **8**(5): p. e10557.
17. Kazakoff, P.W., et al., *An in vitro model for endothelial permeability: assessment of monolayer integrity.* In Vitro Cell Dev Biol Anim, 1995. **31**(11): p. 846-52.
18. Moreno-Arotzena, O., et al., *Characterization of Fibrin and Collagen Gels for Engineering Wound Healing Models.* Materials (Basel), 2015. **8**(4): p. 1636-1651.
19. Bumgarner, J.R. and R.J. Nelson, *Open-source analysis and visualization of segmented vasculature datasets with VesselVio.* Cell Rep Methods, 2022. **2**(4): p. 100189.
20. Hagerling, R., et al., *VIPAR, a quantitative approach to 3D histopathology applied to lymphatic malformations.* JCI Insight, 2017. **2**(16).
21. Kirst, C., et al., *Mapping the Fine-Scale Organization and Plasticity of the Brain Vasculature.* Cell, 2020. **180**(4): p. 780-795 e25.
22. Spangenberg, P., et al., *Rapid and fully automated blood vasculature analysis in 3D light-sheet image volumes of different organs.* Cell Rep Methods, 2023. **3**(3): p. 100436.
23. Weinkamer, R., P. Kollmannsberger, and P. Fratzl, *Towards a Connectomic Description of the Osteocyte Lacunocanalicular Network in Bone.* Curr Osteoporos Rep, 2019. **17**(4): p. 186-194.